Graphical Abstract

Simulation and automation of aluminium panel shot peen forming

Vladislav Sushitskii, Pierre-Olivier Dubois, Hong Yan Miao, Martin Lévesque, Frédérick P. Gosselin

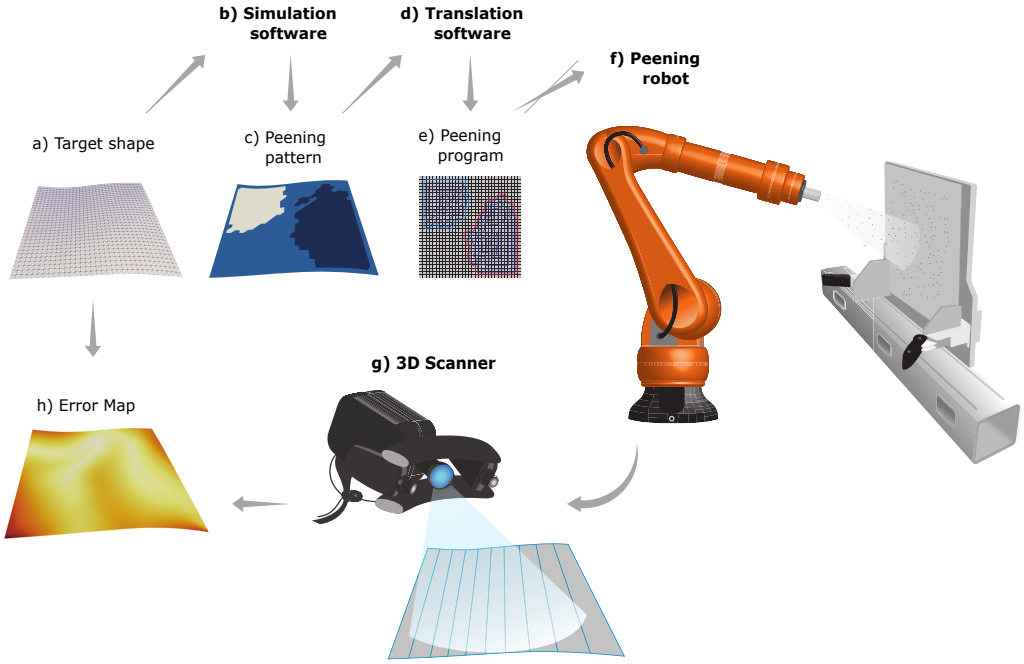

Simulation and automation of aluminium panel shot peen forming

Vladislav Sushitskii[a,b], Pierre-Olivier Dubois[c], Hong Yan Miao[a,b], Martin Lévesque[a], Frédérick P. Gosselin[a,b]

[a] *Laboratory for Multiscale Mechanics (LM2), Department of Mechanical Engineering, Polytechnique Montreal, 2500 Chemin de Polytechnique, Montreal, H3T1J4, Quebec, Canada*
[b] *Aluminium Research Centre – REGAL, 1065 Avenue de la Médecine, Quebec, G1V0A6, Quebec, Canada*
[c] *Aerospace Technology Center (CTA), Saint-Hubert, J3Y8Y9, Quebec, Canada*

Abstract

We present a methodology for automated forming of metal plates into freeform shapes using shot peening. The methodology is based on a simulation software that computes the peening pattern and simulates the effect of its application. The pattern generation requires preliminary experimental characterization of the treatment. The treatment is applied by a shot peening robot. The program for the robot is generated automatically according to the peening pattern. We validate the methodology with a series of tests. Namely, we form nine aluminum plates into doubly curved shapes and we also shape model airplane wing skins. The article describes the complete workflow and the experimental results.

Keywords: Shot peen forming, Non-Euclidean plates, Eigenstrains, Optimization, Modeling, Automation

Email addresses: vladislav.sushitskii@polymtl.ca - corresponding author (Vladislav Sushitskii), po.dubois@cegepmontpetit.ca (Pierre-Olivier Dubois), hong-yan.miao@polymtl.ca (Hong Yan Miao), martin.levesque@polymtl.ca (Martin Lévesque), frederick.gosselin@polymtl.ca (Frédérick P. Gosselin)

1. Introduction

Shot peen forming (peen forming) is an industrial process for forming metal plates into smoothly curved shapes. It consists in projecting a stream of rigid particles (shot) towards a metal plate surface at high velocity. Numerous overlapping impacts induce plastic expansion of the outer layer of material, which causes bending of the plate in the treated segment. The set of treated segments over the flat plate surface is called the peening pattern. Altering the pattern shape or the treatment effectiveness alters the deformed shape as well. This versatility makes peen forming an efficient instrument for achieving complex curvature profiles on large plates, such as airplane wing skins [1] or rocket tank bulkheads [2].

Nowadays, the market proposes a wide range of programmable peen forming robots, such as those mentioned in Ref. [3] and [4]. Nevertheless, there exists no publicly accessible numerical tool that would automatically control a peening robot, bridging the gap between the numerical model (CAD) and the robot path. Such a tool must generate an optimal peening pattern for a given target shape, i.e., solve the *inverse problem*, then translate the pattern into a program for the peening robot, and simulate the effect of its application, i.e., solve the *forward problem*. At least one commercial company claims to have developed an appropriate tool, but the adopted approach is confidential [3][5]. Smaller companies thus use manual peen forming, which is cheaper but less efficient. It is a trial-and-error process that provides lower repeatability than the automated one. The quality of forming in this case relies completely on the operator's experience, which involves costly training. Moreover, it can lead to chronic health problems for the operator [5].

In the matter of peen forming simulation, a straightforward modelling of every impact would be computationally unachievable for the case of large industrial parts [6]. However, the simulation can be accelerated by means of the *eigenstrain* representation of the peening-induced loads [7]. In the peen forming case, it implies formulating the loads as an anelastic strain (eigenstrain) introduced in the treated segments analogous to thermal expansion, so that the individual impacts are not simulated [8][9]. The deformation of the plate caused by the eigenstrain is described as the elastic material response, i.e., the springback [10]. It can be computed using the shell finite element method [9][11]. This method can also be reformulated in terms of the theory of non-Euclidean plates [12], which is specifically designed to describe the reconfiguration of plates subjected to eigenstrain. The eigenstrain approach

together with the theory of non-Euclidean plates provide a framework for the inverse problem resolution [13].

In terms of the eigenstrain approach, the peening pattern is described by the eigenstrain magnitude and its distribution over the surface of the plate. However, from a practical point of view, the pattern is described by the shot stream parameters and by the shape of the treated segment. The eigenstrain magnitude can be related with the shot stream parameters through direct impact simulation on a small representative volume of material [6][14]. This requires building a specific simulation model that reflects plastification of material induced by the impacts. Otherwise, the eigenstrain can be quantified experimentally using small specimens made of the same material as the plates subjected to forming. The specimens must be uniformly treated with the same parameters that are applied for treatment of the plates. The peening-induced plastic strain, i.e., eigenstrain, is either measured directly using X-ray diffraction [15], or computed based on the residual stress measurements [9]. These strategies require costly measuring equipment and can be replaced by an eigenstrain-based simulation software. Indeed, in such case the eigenstrain is deduced from the deflection of a uniformly treated specimen [16][17]. More precisely, the eigenstrain is adjusted in the way that the simulated deflection corresponds to the measured one. Although this method does not allow reconstructing the full residual stress profile, it allows quantifying the macroscopic bending and stretching induced by the treatment, and since it does not require any specific equipment or numerical models, it can be efficiently applied in industry.

The eigenstrain induced in an aluminum plate by a perfectly symmetrical impact can be anisotropic [18]. The main causes for this effect are the material plastic anisotropy [19][20] and the initial stresses induced by the fabrication process [21][22]. Another potential cause is the prestress, i.e., pre-bending of the plate with clamping supports during peening, which is not present if the plate is held flat during treatment. The influence of the three causes can be quantified experimentally using an additional equipment [22]. Otherwise, the eigenstrain anisotropy can be characterized using an eigenstrain-based simulation software, so that the anisotropy is numerically adjusted to fit the simulations to the experiments. In terms of this method, a particular challenge lies in the fact that the influence of the eigenstrain anisotropy on the final shape depends on the geometry of the plate [22]. Consequently, the characterization should ideally be done using exactly the same plates as those that are supposed to be shaped afterwards.

Precise reproduction of the peening pattern shape is crucial for the process efficiency. One possible approach implies masking of the untreated segments with subsequent uniform treatment of the plate. The masks are glued to the surface of the plate to absorb the energy of the shot and to protect the material underneath. A thick adhesive tape or cardstock cope well with this task. The masks are shaped either manually or using a laser cutter and are manually glued to the component [21][23]. This approach is cumbersome when the applied pattern changes from one component to another, because a different mask needs to be fabricated for each pattern. For this reason, an automated peen forming system would require a different approach to remove this manual and time consuming component of the workflow.

In the existing literature on shot peen forming, the experimental validation of the numerical forward problem resolution is mostly limited to uniform treatment of small coupons [17][24]. Such experiments do not require an automated peen forming system due to the simplicity of the applied pattern. Moreover, the existing literature on the numerical inverse problem resolution in this domain is mostly limited to the description of the developed algorithms [25] or to their numerical validation [11][13]. Only Faucheux et al. have validated their inverse problem resolution strategy experimentally on complex shapes such as a cylinder, a saddle and a wave [21][23]. The peening patterns in this research were applied using masking, so the overall peen forming workflow is not completely automated. Moreover, the developed deflection was of the order of millimeters for 1×1 m panels, which is too small to reveal nonlinear geometric effects appearing with large deflections.

Here, we present a fully automated peen forming workflow implying a programmable peening robot. We describe the numerical tools, the steps for their calibration and the specifically designed installations for the robot. The numerical tools include the simulation software and the translation software. The former solves both the forward and the inverse problems and allows to quantify the eigenstrain anisotropy. The latter automatically converts the peening pattern into the nozzle paths. Hence, the shot stream "paints" the peening pattern on the plate, so the necessity for masking is eliminated. Together, the numerical tools form a "CAD-to-path" solution allowing the user to input a desired shape and to generate the robot program with a minimal intervention.

The automated workflow was developed for experimental validation of the numerical forward and inverse problem solvers described in Ref. [13]. The forward problem solver validation involves randomly generated and strongly

curved target shapes that have deflection of $10-31$ mm. The inverse problem solver validation consists in shaping parts of a model airplane wing skin of a predefined geometry.

2. Methodology

The methodology section begins with a description of the underlying principles of our simulation software. Next, we present the translation software and the peen forming robot. We then examine our strategy for the estimation of the experimental error implying 3D scanning. Subsequently, we describe the experimental steps for the software calibration. They include characterization of the shot stream, determination of the eigenstrain induced by a given treatment and quantification of the eigenstrain anisotropy on a given component. All the elements mentioned above constitute together the automated peen forming workflow, which is schematized in Figure 1. The end of the methodology section is dedicated to the experimental validation of the forward and the inverse problem solvers.

2.1. The simulation software

2.1.1. Representation of peening-induced loads with eigenstrain

Following Ref. [13], we virtually divide the plate into two layers of equal thickness to simulate the curving effect of peen forming. We assign in-plane swelling to one layer and in-plane shrinking to the other in the spots where the plate is treated. The swelling layer is located on the side that undergoes treatment. The swelling and shrinking are assigned in the form of eigenstrain and are analogous to thermal expansions [9]. The eigenstrain magnitude is constant in the through-thickness direction for each layer but varies along the plate surface according to the peening pattern. We denote the eigenstrain tensors imposed on the top and bottom layers as $\boldsymbol{\varepsilon}^t$ and $\boldsymbol{\varepsilon}^b$ respectively. The incompatibility between $\boldsymbol{\varepsilon}^t$ and $\boldsymbol{\varepsilon}^b$ forces the plate to bend.

We endow the component with Lagrangian coordinates x, y, z, where the $x-$ and $y-$axes follow the plate mid-surface. Both eigenstrain tensors in these coordinates have the following form [21]:

$$\boldsymbol{\varepsilon}^j = \begin{pmatrix} \varepsilon^j_{xx} & 0 & 0 \\ 0 & \varepsilon^j_{yy} & 0 \\ 0 & 0 & -(\varepsilon^j_{xx} + \varepsilon^j_{yy}) \end{pmatrix} \quad \text{for} \quad j = t, b. \tag{1}$$

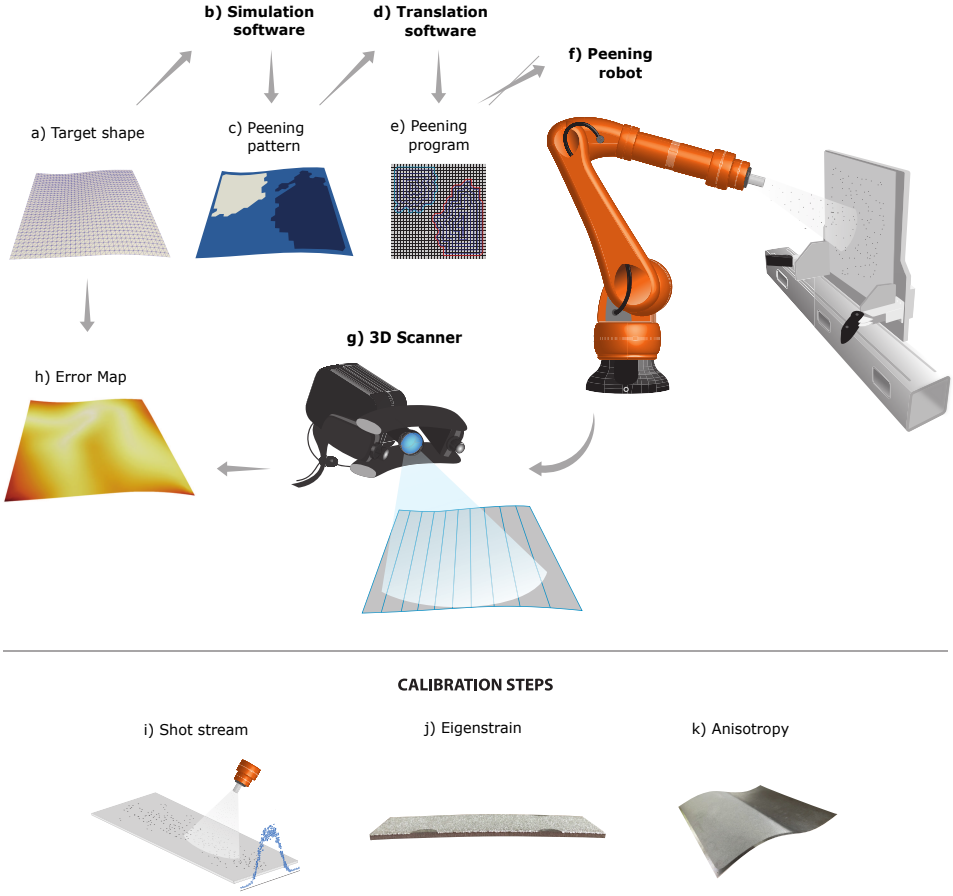

Figure 1: Schematic overview of the automated shot peen forming workflow. The numerical model of the target shape (a) is input into the simulation software (b). The latter computes an optimal peening pattern (c), that must be applied to form the plate into the target shape. The peening pattern is input into the translation software (d), which generates the peening program (e). The peening program includes the nozzle paths and a set of peening parameters that allow the peening robot (f) to reproduce the peening pattern. The peening program is loaded into the peening robot in the form of a programming code. When the treatment is finished, we characterize the curved shape of the plate using a 3D scanner (g) and trace an error map (h), which shows discrepancy between the target and the scanned shapes. The simulation and the translation softwares require experimental calibration, which consists in characterizations of the shot stream (i), of the eigenstrain (j) induced by the peening treatment, and of the eigenstrain anisotropy (k). The shot stream is characterized with flat dummy specimens, the eigenstrain is measured using 76×19 mm aluminum coupons, and the anisotropy is quantified with the help of square aluminum plates. Art by IMPAKT Scientifik

For a plate with uniform properties and initial stresses, the proportion between ε^j_{xx} and ε^j_{yy} is constant along the whole component. It is expressed with the *anisotropy coefficient* χ [22]:

$$\begin{cases} \varepsilon^j_{xx} = (1+\chi)\varepsilon^j_*, \\ \varepsilon^j_{yy} = (1-\chi)\varepsilon^j_*, \end{cases} \qquad \text{for} \quad j = t, b, \tag{2}$$

where $\varepsilon^j_* = (\varepsilon^j_{xx} + \varepsilon^j_{yy})/2$. If the material is plastically isotropic and free of stresses then $\varepsilon^j_{xx} = \varepsilon^j_{yy} = \varepsilon^j_*$.

2.1.2. Geometrical shape description

Provided that peen forming deals with thin plates, we associate the plate shape with the shape of its mid-surface. We numerically discretize the mid-surface with triangular elements. Following Ref. [26], we describe the shape of each element with two matrices: **a** and **b**. The former represents the local first fundamental form and the latter represents the local second fundamental form, that respectively characterize the local stretching and the local curvature [27]. The set of fundamental forms computed for each element uniquely describes the shape of a triangulated surface. For a triangular element defined by vertices $\vec{v}_0$, $\vec{v}_1$, $\vec{v}_2$ and edges $\vec{e}_0 = \vec{v}_1 - \vec{v}_0, \vec{e}_1 = \vec{v}_2 - \vec{v}_1$, $\vec{e}_2 = \vec{v}_0 - \vec{v}_2$ the two matrices are computes as:

$$\mathbf{a} = \begin{bmatrix} \vec{e}_1 \cdot \vec{e}_1 & \vec{e}_1 \cdot \vec{e}_2 \\ \vec{e}_2 \cdot \vec{e}_1 & \vec{e}_2 \cdot \vec{e}_2 \end{bmatrix}; \tag{3}$$

$$\mathbf{b} = \begin{bmatrix} \vec{e}_1 \cdot 2(\vec{n}_0 - \vec{n}_2) & -\vec{e}_1 \cdot \vec{n}_0 \\ -\vec{e}_1 \cdot \vec{n}_0 & \vec{e}_2 \cdot 2(\vec{n}_1 - \vec{n}_0) \end{bmatrix}. \tag{4}$$

Here, $\vec{n}_i$ stands for a vector normal to the edge $\vec{e}_i, i = 1, 2, 3$. The angle of inclination of $\vec{n}_i$ with respect to the plane enclosing the triangular element is variable and thus allows a more flexible shape description. Figure 2 illustrates the components of a triangular element that participate in computation of the fundamental forms.

The local principal curvatures can be computed for each element as the eigenvalues of the shape operator $\boldsymbol{S} = \mathbf{a}^{-1}\mathbf{b}$ [28][29]. The local mean curvature H is the average of the two principal curvatures, and the curvature along any direction may be deduced from the principal curvatures using Euler's formula [28].

2.1.3. The forward problem resolution

In terms of peen forming, the forward problem consists in the determination of the deformed shape of the component provided with the eigenstrain pattern. For this, we rely on the approach presented in Ref. [26]. We assume that the plate is free to deform and that the treatment is applied instantly from both sides. We also assume that the initial configuration is flat, and we denote the initial lengths of the element edges as $\vec{e}_0$, $\vec{e}_1$, $\vec{e}_2$. We consider the eigenstrain constant inside a triangular element. An anisotropic eigenstrain $(\varepsilon_{xx}, \varepsilon_{yy})$ prescribes new *rest* edges $\vec{e}_0^{\,r}$, $\vec{e}_1^{\,r}$, $\vec{e}_2^{\,r}$:

$$\vec{e}_i^{\,r} = (\varepsilon_{xx} + 1)\vec{e}_{ix} + (\varepsilon_{yy} + 1)\vec{e}_{iy} \quad \text{for} \quad i = 1, 2, 3. \tag{5}$$

Here, $\vec{e}_{ix}$ is the projection of $\vec{e}_i$ on the x-axis and $\vec{e}_{iy}$ is the projection of $\vec{e}_i$ on the $y-$axis. New edges induce a new *rest* first fundamental form $\mathbf{a}_r$:

$$\mathbf{a}_r = \begin{bmatrix} \vec{e}_1^{\,r} \cdot \vec{e}_1^{\,r} & \vec{e}_1^{\,r} \cdot \vec{e}_2^{\,r} \\ \vec{e}_2^{\,r} \cdot \vec{e}_1^{\,r} & \vec{e}_2^{\,r} \cdot \vec{e}_2^{\,r} \end{bmatrix}. \tag{6}$$

A different eigenstrain $(\varepsilon_{xx}^t, \varepsilon_{yy}^t)$ and $(\varepsilon_{xx}^b, \varepsilon_{yy}^b)$ imposed on the top and bottom layers respectively induce different first fundamental forms $\mathbf{a}_{r,t}$ and $\mathbf{a}_{r,b}$. Concurrently, all components of the rest second fundamental forms $\mathbf{b}_{r,t}$ and $\mathbf{b}_{r,b}$ equal zero because the edge normals stay perpendicular to the plane englobing the flat initial configuration.

Prescription of a different eigenstrain to the top and bottom layers does not make the plate delaminate. Instead, the plate adopts a curved configu-

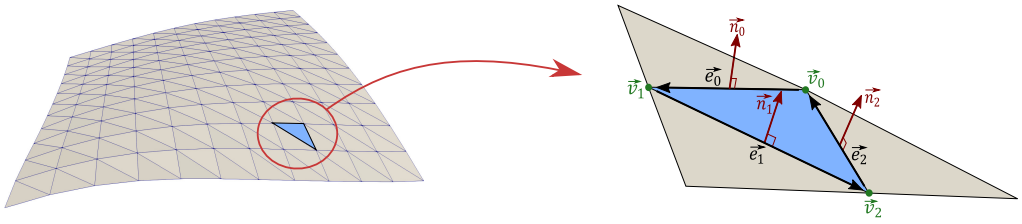

Figure 2: A triangular mesh element and the vectors serving for computation of the local fundamental forms. The vectors $\vec{v}_0$, $\vec{v}_1$, $\vec{v}_2$ define positions of the element vertices in the global coordinate system. The edge vectors $\vec{e}_0$, $\vec{e}_1$, $\vec{e}_2$ are computed as the difference between the corresponding vertex vectors. The vectors $\vec{n}_0$, $\vec{n}_1$, $\vec{n}_2$ are traced in the center of the corresponding edges and define the local curvature of the mesh. They are normal to the edges, but their angle of inclination with respect to the element constitutes a degree of freedom.

ration described with the *final* fundamental forms $\mathbf{a}_f$ and $\mathbf{b}_f$. Hence, from the mathematical point of view, the forward problem resolution consists in the determination of $\mathbf{a}_f$ and $\mathbf{b}_f$ taking $\mathbf{a}_{r,t}$ and $\mathbf{a}_{r,b}$ as the input. This is done through numerical minimization of the global elastic energy functional E_{BL} [13]:

$$\begin{aligned} E_{BL} = \frac{1}{2}\sum_{k=1}^{K}\Bigg[&\frac{h}{8}\big\|(\mathbf{a}_{r,b}^{-1})_k(\mathbf{a}_f)_k - \mathbf{I}\big\|_e^2 + \frac{h^3}{24}\big\|(\mathbf{a}_{r,b}^{-1})_k(\mathbf{b}_f)_k\big\|_e^2 \\ &+\frac{h^2}{8}\Big\langle\big((\mathbf{a}_{r,b}^{-1})_k(\mathbf{a}_f)_k - \mathbf{I}\big), (\mathbf{a}_{r,b}^{-1})_k(\mathbf{b}_f)_k\Big\rangle_e\Bigg]\sqrt{\det(\mathbf{a}_{r,b})_k} \\ &+\frac{1}{2}\sum_{k=1}^{K}\Bigg[\frac{h}{8}\big\|(\mathbf{a}_{r,t}^{-1})_k(\mathbf{a}_f)_k - \mathbf{I}\big\|_e^2 + \frac{h^3}{24}\big\|(\mathbf{a}_{r,t}^{-1})_k(\mathbf{b}_f)_k\big\|_e^2 \\ &-\frac{h^2}{8}\Big\langle\big((\mathbf{a}_{r,t}^{-1})_k(\mathbf{a}_f)_k - \mathbf{I}\big), (\mathbf{a}_{r,t}^{-1})_k(\mathbf{b}_f)_k\Big\rangle_e\Bigg]\sqrt{\det(\mathbf{a}_{r,t})_k}. \end{aligned} \tag{7}$$

Here, the index k is attributed to the fundamental forms belonging to the element k, and K denotes the total number of elements in the model. The matrix $\mathbf{I}$ is the 2×2 identity matrix. The elastic norm $\|\cdot\|$ and the elastic energy inner product $\langle\cdot,\cdot\rangle$ denote the following operations:

$$\big\|\mathbf{A}\big\| = \alpha Tr^2(\mathbf{A}) + 2\beta Tr(\mathbf{A}^2), \tag{8}$$

$$\big\langle\mathbf{A},\mathbf{B}\big\rangle = \alpha Tr(\mathbf{A})\,Tr(\mathbf{B}) + 2\beta Tr(\mathbf{AB}), \tag{9}$$

where $\mathbf{A}$ and $\mathbf{B}$ are arbitrary matrices, $\alpha = Y\nu/(1-\nu^2)$ and $\beta = Y/(2+2\nu)$. The values ν and Y stand respectively for the Poisson's ratio and the Young modulus of the treated material.

We minimize the elastic energy functional with the help of the Limited-memory Broyden–Fletcher–Goldfarb–Shanno (L-BFGS) optimization algorithm [30] using the analytically computed gradients [31].

2.1.4. The inverse problem resolution

In terms of peen forming, the inverse problem consists in the determination of the eigenstrain tensors $\boldsymbol{\varepsilon}^t$ and $\boldsymbol{\varepsilon}^b$ imposed on each element taking the target shape as input. Another necessary input is the initial shape geometry. Our algorithm for the inverse problem resolution relies on full consistency between the initial and the target meshes. For this reason, the initial mesh

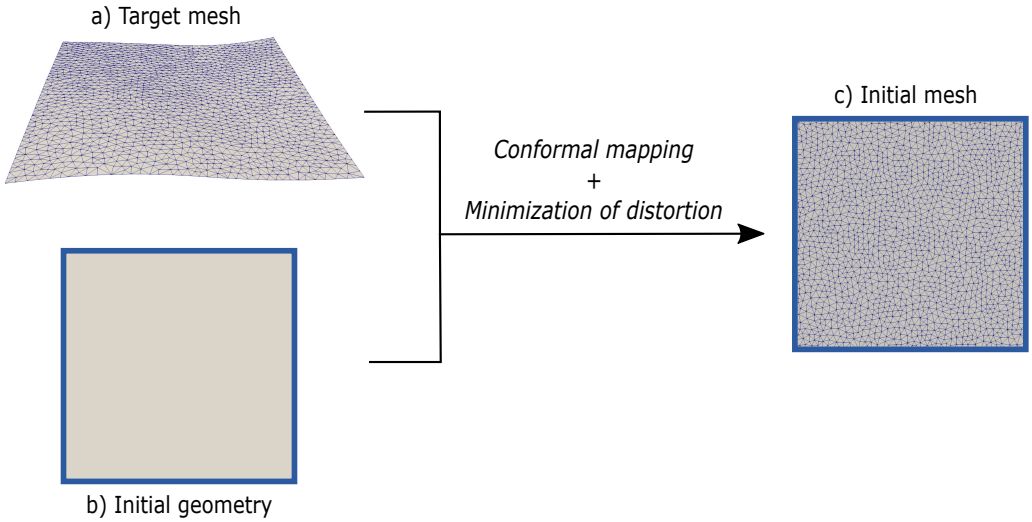

Figure 3: Generation of the initial mesh. The mesh of the curved target shape (a) is projected on the flat initial geometry (b) using the LSCM algorithm. The distortion of each element in the projected mesh is then minimized with respect to the target mesh using the L-BFGS algorithm. The resulting mesh (c) is used as the initial mesh during the inverse problem resolution.

is generated as a function of the target mesh, which is illustrated in Figure 3. It is done in two steps. Firstly, the target mesh is projected on the initial geometry using the Least Squares Conformal Mapping (LSCM) algorithm [32]. Secondly, the initial vertex positions are numerically optimized using the L-BFGS algorithm to minimize the element distortion with respect to the target mesh. The initial shape boundary is kept fixed during the optimization.

The target shape is described with two fundamental forms $\mathbf{a}_{tar}$ and $\mathbf{b}_{tar}$. Our algorithm for the inverse problem resolution is iterative. Each iteration implies an adjustment of the eigenstrain pattern and subsequent computation of the new current shape provided by the adjusted pattern. The eigenstrain tensors are adjusted for each triangular element separately based on comparison of the current shape with the target shape. More precisely, on each iteration, we multiply ε_*^t and ε_*^b by the ratio between the local mean curvatures of the target shape H_{tar} and of the current shape H_c:

$$\varepsilon_*^{j,new} = \varepsilon_*^j \frac{H_{tar}}{H_c} \quad \text{for} \quad j = t, b. \tag{10}$$

Next, we solve the forward problem for $(\varepsilon_*^{t,new}, \varepsilon_*^{b,new})$ and thus obtain a new current shape. These two steps are repeated until stabilization of the current shape. The anisotropy coefficient χ is pre-defined with a calibration step described in Section 2.5.3 and kept constant throughout the iterations.

The initial guess is made in terms of $\mathbf{a}_{r,t}$ and $\mathbf{a}_{r,b}$ as presented in Ref. [13]. Thus, we first compute the $\mathbf{a}_{r,t}$ and $\mathbf{a}_{r,b}$ as:

$$\begin{cases} \mathbf{a}_{r,t} = \mathbf{a}_{tar} - \frac{2h}{3}\mathbf{b}_{tar}, \\ \mathbf{a}_{r,b} = \mathbf{a}_{tar} + \frac{2h}{3}\mathbf{b}_{tar}. \end{cases} \tag{11}$$

Then, for each layer, we take the average of the eigenstrains prescribed by $\mathbf{a}_{r,t}$ and $\mathbf{a}_{r,b}$ in each direction and use this eigenstrain as the initial guess.

This algorithm constitutes a simplified version of that described in Ref. [13]. Namely, the eigenstrain is adjusted in the way that it leads to the target *curvature*, but the *stretching* of the target shape is not taken into account. This formulation was adopted because the target shapes implied large rotations but small stretch with respect to the initial state.

The final step of the inverse problem resolution is the pattern grouping [13], which is done after the last iteration. The aim of this process is to split the peening pattern into segments treated with practically attainable peening regimes. Each attainable peening regime is related to the corresponding induced eigenstrain during the calibration phase. The grouping algorithm takes the eigenstrain assigned to each element and reassigns it the closest eigenstrain among the limited number of attainable ones. This removes gradual variation of the eigenstrain along the plate surface and divides the pattern into strictly defined peened segments. When the grouped pattern is computed, we solve the forward problem taking this pattern as input. This step serves for preliminary estimation of the error between the target shape and the final shape developed with the ready-to-use pattern.

2.1.5. Inverse identification of the anisotropy coefficient

This problem is similar to the inverse problem, except for the condition that the local eigenstrains ε_*^t and ε_*^b are pre-defined and the anisotropy coefficient χ must be determined. We assume that χ is a global property of the treated material, so it is uniform along the plate surface. The initial mesh is generated based on the target mesh in the same way as it is done during the inverse problem resolution.

The problem is solved through the iterative adjustment of χ based on the comparison of the current and target shapes. We compute local curvatures along the x-direction for both shapes: κ_x^c for the current shape and κ_x^{tar} for the target shape. We average their absolute values κ_{avg}^c and κ_{avg}^{tar} and then adjust χ as follows:

$$\chi^{new} = (1 + \chi)\frac{\kappa_{avg}^{tar}}{\kappa_{avg}^c} - 1. \tag{12}$$

We then adjust the local eigenstrain tensors according to Eqn. (2) and solve the forward problem. Starting with an initial guess of $\chi = 0$, the process is repeated until the convergence of κ_{avg}^c and κ_{avg}^{tar}, providing us with an evaluation of the anisotropy coefficient χ.

2.2. The translation software

The translation software fills the gap between the numerical peening patterns and the actual peen forming process. The peening pattern that it takes as input is provided in the form of a mesh with the eigenstrain assigned to each of the elements. The pattern is divided into segments with different prescribed eigenstrain that correspond to treatment with different peening regimes. The relation between each peening regime, i.e., each set of the peening parameters, and the corresponding eigenstrain is defined during the calibration phase and saved in the software. The software first detects borders of the segments treated with the same peening regime. It then generates the nozzle paths that fill each segment and assigns the peening parameters corresponding to each segment. Finally, the software wraps up the paths and the peening parameters in a programming script written in Karel programming language [33], which is then loaded in the peening robot. The script controls all parameters of the robot operation and does not require any manual adjustment.

The translation software is able to fulfill a peened segment with two types of nozzle paths, which are presented in Figure 4. The first path type is called "Zigzag" and implies straight parallel nozzle paths. The second type is called "Circular". The paths generated in this way constitute a set of concentric closed lines, and the longest line is the outline of the treated segment. The "Circular" paths better fill complexly shaped segments. However, the neighboring paths of this type may not always have a constant offset, that results in a less uniform coverage.

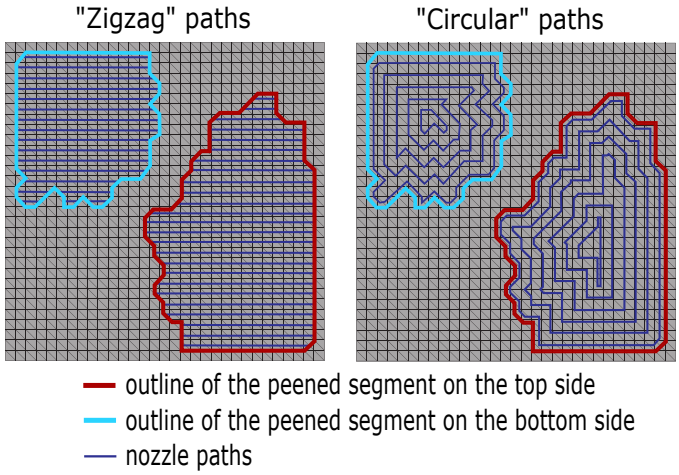

Figure 4: Two types of nozzle paths generated by the translation software. The example pattern implies treatment from the top and bottom sides with the same peening regime.

The software allows adjusting several common parameters for both path types. Thus, the outline of the treated segment can be smoothed with respect to its actual border prescribed by the peening pattern. This allows filtering out features too small to peen with respect to the shot stream width. Moreover, the outline can be offset with respect to the border, which allows scaling the peened segment without resorting to the simulation software. The offset between the paths can also be adjusted depending on the shot stream width, which is measured during the calibration phase. The path offset is adjusted in the way that the peening coverage in the treated segment is as uniform as possible. Figure 5 illustrates the adjusted outline and the concept of the path offset. The speed of movement of the nozzle along the peening paths can also be adjusted depending on the peening regime and is usually set to 50-100 mm/s. The peening robot is not able to block the shot stream during the program execution, so the nozzle moves between different peened segments and different paths inside one segment at a high speed of 1 500 mm/s.

2.3. The peening robot

The peening robot involved in the experiments is based on a Canablast shot peening machine. It possesses a FANUC M20iA programmable robotic arm, which guides the peening nozzle. The robotic arm and the treated component are installed inside a closed peening cell shown in Figure 6.

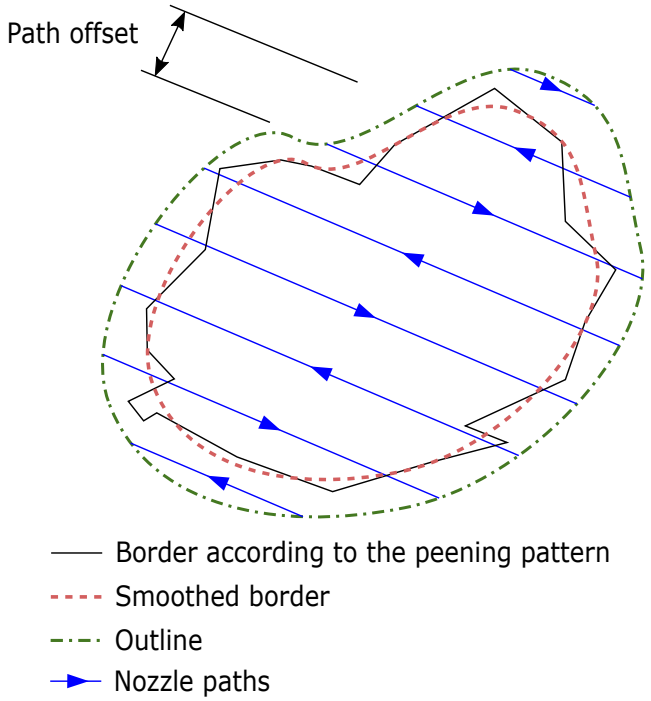

Figure 5: Adjustment of the peened segment executed with the translation software. The outline of the peened segment is smoothed with respect to its initial border and offset to increase the size of the treated segment. The path offset is adjusted to ensure uniform coverage.

We developed a specific peen forming fixture to treat square panels of 320×320 mm. The fixture is designed in two main parts: the fixed and the removable frames. The first ensures a precise location of the peened part in terms of the robot's reference frame and the latter clamps the plate along its perimeter. This system eases the installation process and allows removing the plate from the shot peening cell while keeping it under the clamping constraints.

The fixture is mounted on a rotary axis, so the plate can be treated from both sides with no need for manual reinstallation. The rotary axis turns the plate by 180° in 2 seconds, and during this process the programming script points the nozzle aside, that prevents undesired impacts.

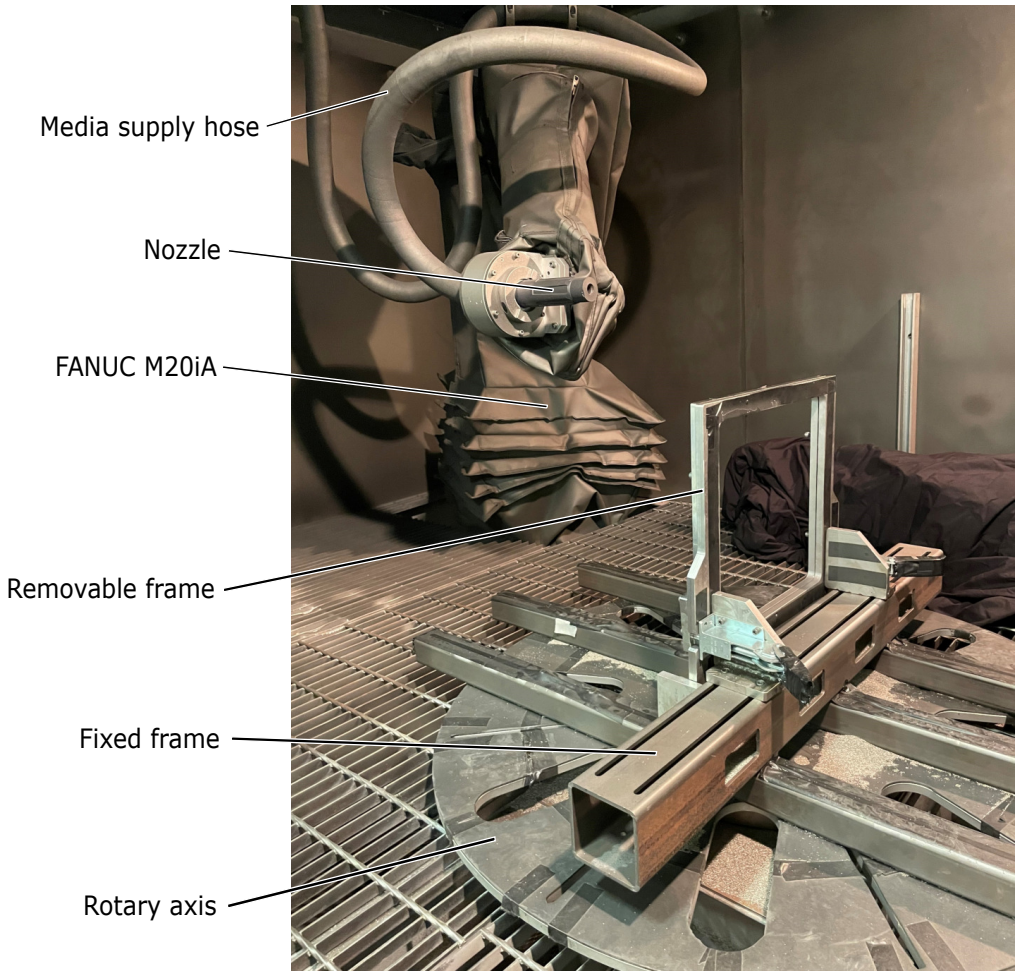

Figure 6: The interior on the robotic peen forming cell. The programmable robtic arm FANUC M20iA giudes the peening nozzle, and the media is supplied to the nozzle through the elastic hose. The treated plate is clamped by the removable frame along its perimeter. The removable frame is mounted on the fixed frame attached to the rotary axis.

2.4. 3D scanning and error map

Once a plate is treated, we compare its curved shape with numerical prediction. We remove the plate from the frame and we scan it using a Hexagon StereoScan neo 3D scanner. Before scanning, the plate is covered with Magnaflux SKD-S2 aerosol to make its surface non-reflective. The result of 3D scanning is a meshed surface describing the plate shape.

Next, we numerically superimpose each scanned shape with the corresponding predicted shape and we compute the Hausdorff distance d_H [34] between the two shapes. We nondimensionalize the Hausdorff distance by dividing it by the deflection of the target shape Δz, which is computed as the smallest dimension of a box bounding the plate. Thus, we obtain a nondimensionalized error Ω_z:

$$\Omega_z = \frac{d_H}{\Delta z}. \tag{13}$$

Figure 7 illustrates the workflow for determining Ω_z. The optimal alignment of the two shapes is done through least squares estimation of the transformation parameters [35].

2.5. Calibration steps

2.5.1. The shot stream characterization

We first estimate the shot stream intensity for each peening regime that we use. It is done following the standard procedure involving type A Almen strips and the Almen gage [36]. Each peening regime used for the treatment of the plates is applied until saturation, and the intensity measurement is necessary to estimate the appropriate number of nozzle passages. In other words, we estimate how many times the nozzle must pass along the paths prescribed by the translation software to achieve saturation in the whole treated segment.

The nozzle paths are lines that direct the center of the nozzle, but the actual shot stream has a finite width. Hence, we measure the distribution of shot inside the stream to define the nozzle path offset. It is mainly influenced by the distance from the nozzle to the treated component. We perform this test using a 418 × 127 mm flat dummy specimens. We make one peening passage in the center of the specimens along the longitudinal direction translating the nozzle at a high speed of 1 500 mm/s and then scan the specimen with a document scanner. Next, we post process the scanned image, i.e.,

we highlight the white pixels corresponding to impacts and we darken the background corresponding to the untreated surface. The picture resolution is 4830×1470 pixels, and we count the number of white pixels in each pixel column out of 1470. Figure 8 shows an example of the shot distribution measured in this way. We set the paths offset to the largest value that ensures uniform coverage of the treated segment with a maximal variation in coverage of 1%. This value equals approximately half of the shot stream width but is specific for each particular distribution.

2.5.2. Determination of the eigenstrain

Every combination of peening regime and treated material induces different ε_*^t and ε_*^b. We determine ε_*^t and ε_*^b experimentally using rectangular coupons of size 76×19 mm. The coupons are cut with waterjet cutting from the same aluminum plates as those that are shaped afterwards. The coupons are clamped in the Almen holder and treated until saturation.

The bending behavior of the coupon is governed by the dimensionless

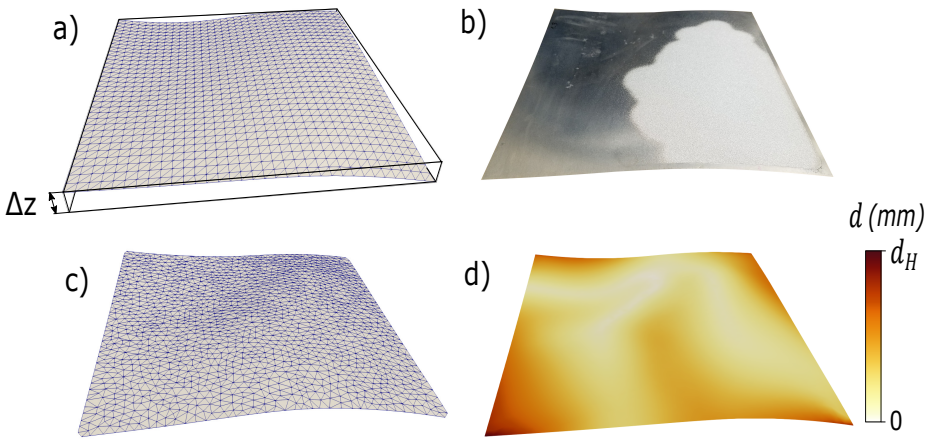

Figure 7: Determination of the dimensionless error $\Omega_z = d_H/\Delta z$ between the simulated shape and the shape of the treated plate. a) The simulated shape and its bounding box. The deflection Δz is computed as the smallest dimension of the bounding box. b) A photo of the plate treated following the computed pattern that leads to the simulated shape. The non-reflective surface is the treated part. c) The meshed shape scanned with a 3D scanner. d) Map of the local distances d between the simulated and the scanned shapes that were optimally aligned. The map is traced on the simulated shape. The Hausdorff distance d_H is the maximal value of local distances d.

load Γ_B [22]:

$$\Gamma_B = \frac{3}{2}(1+\nu)\Delta\varepsilon, \tag{14}$$

where $\Delta\varepsilon = \varepsilon_*^t - \varepsilon_*^b$. For small values of Γ_B, the curvature κ measured at the center of the treated coupon is the same in any direction. Moreover, in this case the load Γ_B is proportional to the dimensionless curvature κh [22]. The treated coupon has a convex shape (κ is negative), and the relation takes the form:

$$\kappa h = -\mu\Gamma_B. \tag{15}$$

The proportionality constant μ can be determined using numerical simulations (see Appendix A). Therefore, $\Delta\varepsilon$ can be deduced from κ. According to the simulations, the linear relation holds at least up to $\Gamma_B = 8 \times 10^3$.

The curvature κ, in turn, is deduced from the coupon deflection u, which is measured using the Almen gage [37]. We can approximate the shape of a curved coupon to that of an elliptic paraboloid [38], which allows to express

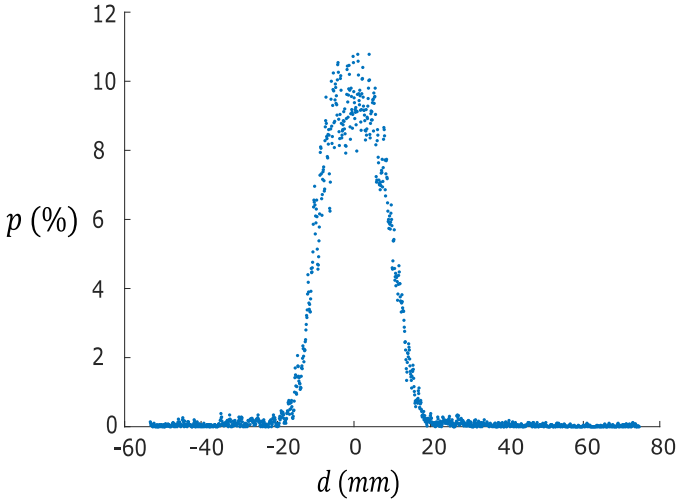

Figure 8: Spatial distribution of shot on a 418 × 127 mm flat dummy specimen that underwent one passage of the peening nozzle in the longitudinal direction. The nozzle travelled at a speed of 1500 mm/s, and the nozzle distance in this case equaled 152.4 mm. The graph indicates the percentage p of the peening-affected surface as a function of the transverse coordinate d. More precisely, we virtually divided the specimen into 1470 columns traced in the longitudinal direction, and the percentage p denotes the ratio of the peening-affected area in each column with respect to its total area.

u as:

$$u = -\kappa \frac{l_x^2 + l_y^2}{2}. \tag{16}$$

Here, l_x=15.87 mm and l_y=7.94 mm are the dimensions of the rectangle formed by the supports of the Almen gage [37].

The dimensionless curvature κh depends on $\Delta\varepsilon$ and does not depend on the sum $(\varepsilon_*^t + \varepsilon_*^b)$ [22]. This sum influences stretching of the plates [13], but shot peening induces small eigenstrain [6][22]. Hence, we conclude that the peening-induced stretching is also small and assume that $\varepsilon_*^t = -\varepsilon_*^b$. Combining Eqn. (14 – 16) we conclude that:

$$\begin{cases} \varepsilon_*^t = \dfrac{2hu}{3\mu(1+\nu)(l_x^2 + l_y^2)}; \\ \varepsilon_*^b = -\dfrac{2hu}{3\mu(1+\nu)(l_x^2 + l_y^2)}. \end{cases} \tag{17}$$

For better stability of the results, we treat four coupons with each regime and compute their average deflection u_{avg}. We then substitute u_{avg} for u in Eqn. (17) and thus find ε_*^t and ε_*^b.

2.5.3. Determination of the anisotropy coefficient

Aluminum plates are produced by rolling, and this process is one of the key factors inducing the eigenstrain anisotropy. Namely, the peening induced eigenstrain is different in the rolling direction (L) and in the in-plane transverse direction (T). This effect alters the local curvatures induced by peening in the L- and T-directions. Thus, if peen forming is simulated assuming that the material is isotropic, then in practice the local curvature in one direction is bigger than that simulated, and the local curvature in the other direction is smaller [22]. A similar effect is also observed during peen forming of metal laminates containing oriented filaments [39].

We quantify the eigenstrain anisotropy using the "wave" experiment. For this, we use the plates that have the same size and are produced in the same way as those used for the forming experiments. We treat two plates following the "wave" pattern illustrated in Figure 9. This pattern consists in treating half of the plate from one side and the other half from the other side. The orientation of the "wave" pattern controls the bending direction of the plate. Hence, for the first plate, the halves are separated along the T-direction

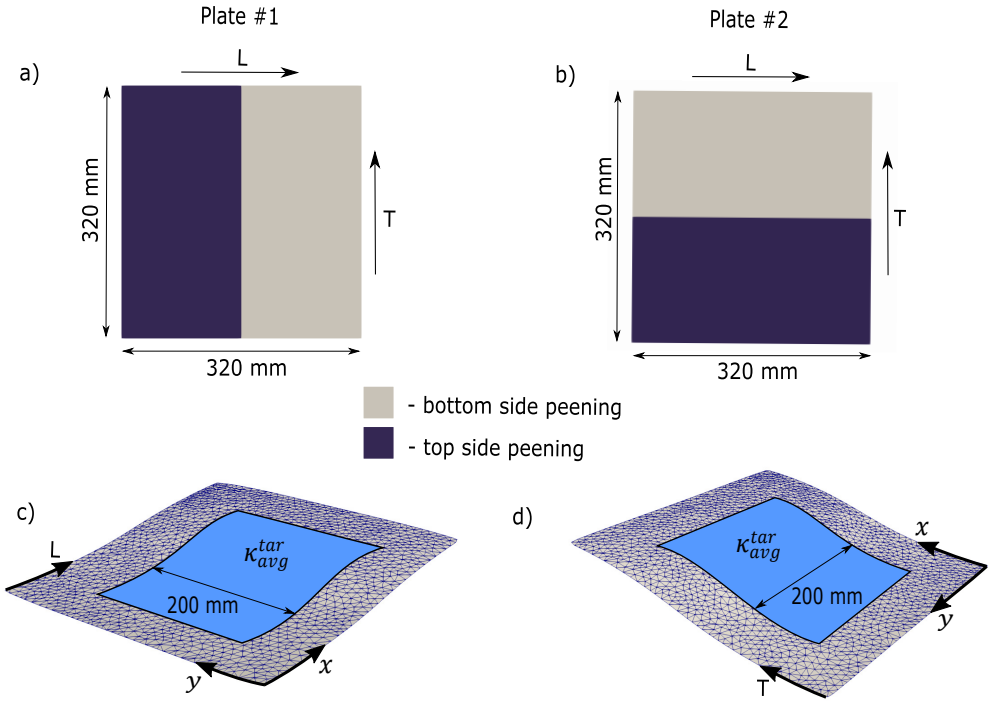

Figure 9: The "wave" experiment. The "wave" peening pattern is applied on two 320 × 320 mm sized aluminum plates. The pattern forces the plates #1 and #2 to bend along the L-direction (a) and the T-direction (b) respectively. The plates are scanned in 3D after peening. Figures c) and d) show the deformed state of the plates #1 and #2 respectively. For each plate, we compute the average absolute value of κ_x for all the elements contained in the 200×200 mm square traced in the center of the plate (blue), and thus obtain κ_{avg}^{tar}.

thus forcing the plate to bend in the L-direction. On the contrary, the same pattern rotated by 90° makes the second plate bend along the T-direction.

We scan both treated plates using the 3D scanner and obtain their meshed numerical models. These models serve as target shapes for numerical determination of the eigenstrain anisotropy coefficient as described in Section 2.1.5. We orient the coordinate system in the way that the x-axis points in the "wave" direction, i.e., in the L-direction for the first plate and in the T-direction for the second plate. To compute the κ_{avg}^{tar}, we take into account only the elements that fall into a 200×200 mm square traced in the center of the plate (see Figure 9). The curvature of the other elements is not taken into account to reduce the influence of the edge effects.

In this way we determine two anisotropy coefficients: χ_L for the first plate and χ_T for the second plate. One of them is positive and the other is negative. We then compute the average of their absolute values $\chi_* = (|\chi_L| + |\chi_T|)/2$ and thus find the eigenstrain anisotropy coefficient for the given material. For the subsequent simulations we make a convention that the x-axis follows the principal eigenstrain direction, so that χ_* is positive.

Theoretically, χ_L must equal $-\chi_T$, so the "wave" treatment of one plate should be sufficient to determine χ_*. However, exact equality is rarely observed because of practical constraints. For example, the simulations do not take into account the initial stresses, which are different for each particular component, or the influence of clamping. For this reason, treatment of two plates stabilizes the measured result and allows to check if ε_*^t and ε_*^b were correctly determined in advance. Moreover, the usage of more than two plates could further improve the precision of this experiment.

2.6. Experimental validation of the simulation software

The experiments consisted in shaping 320 × 320 mm aluminum plates. For this, we fixed six peening regimes described in Table 1. The peening equipment was charged with the cut wire CW28 media having shot diameter of 0.71 mm.

Regime	Mass flow rate (kg/min)	Nozzle distance (mm)	Pressure (kPa)	Intensity (A)	Saturation (Number of passes)
#1	2.27	152.4	248.2	23.5	5
#2		152.4	172.4	19.2	4
#3		152.4	137.9	17	4
#4		152.4	103.4	13.6	4
#5		152.4	68.9	10.9	8
#6		304.8	48.2	8	9

Table 1: Parameters of the peening regimes used in the experimental campaign. The nozzle was oriented perpendicularly to the treated surface. The mass flow rate determines the mass of media that passes through the nozzle. The nozzle distance is the distance from the nozzle to the treated surface. The pressure is created by compressed air. The peening intensity and the number of passes to saturation were measured following the standard procedure using type A Almen strips [36]. The speed of the nozzle travelling was fixed at 100 mm/s.

2.6.1. Validation of the forward problem solver

We shaped nine plates following randomly generated peening patterns and compared the developed shapes with the numerical predictions. The plates were 2.06 mm thick and were made of aluminum 6061-T6. The patterns implied one peening regime listed in Table 1 as #1.

To ensure that each pattern induces a different shape, we generated the patterns based on random target shapes. At first, we generated nine different shapes using the *peaks* function embedded in Matlab programming language. We then solved the inverse problem for each shape and thus obtained the peening patterns. We took into account the measured coefficient of eigenstrain anisotropy, i.e., we imposed the ratio $(1-\chi_*)/(1+\chi_*)$ between the induced eigenstrain in the L- and T-directions.

The target shapes were generated without any constraints on their deflection. The inverse problem solution showed that their development implied much larger eigenstrain magnitude than those achievable with regime #1. Thus, according to the forward problem resolution, the simulated shapes induced by the grouped pattern were less curved than the initially generated target shapes. Consequently, we used these less curved simulated shapes as reference for the experiments.

2.6.2. Validation of the inverse problem solver

The inverse problem resolution was validated using $320 \times 320 \times 1.6$ mm plates made of aluminum 2024-T3. The objective of this validation was to shape parts of the upper and lower skins of a model airplane wing. The wing had constant cross-section in the form of NACA 5430 airfoil [40] with the total chord length of 500 mm (see Figure 10). The two target shapes had the same area as the flat plates: 320×320 mm.

We first solved the inverse problem for both target shapes and obtained the peening patterns. We then solved the forward problem to predict the dimensionless error Ω_z with respect to the target shapes. Next, we translated the peening patterns into programs for the peening robot and treated the aluminum plates. Finally, we compared the experimentally developed shapes with the target shapes constituting the NACA airfoil in terms of Ω_z.

The peening patterns consisted of segments treated with the regimes #2-5 from Table 1. The plates were also uniformly treated from both sides with regime #6 before the application of the peening pattern. Such low intensity pre-treatment is commonly used in industry to enhance the fatigue life of the components. It also makes the surface finishing more uniform.

3. Results

3.1. Calibration steps

The width of the peening-affected band was approximately 4 cm for the nozzle distance of 152.4 mm and approximately 8 cm for the nozzle distance of 304.8 mm. The largest path offsets that provided uniform coverage corresponded to 19 mm and 38 mm respectively.

We determined the eigenstrain using 76×19 mm aluminum coupons (see Section 2.5.2). The 2.06 mm thick coupons made of aluminum 6061-T6 were treated to saturation from one side with regime #1. The 1.6 mm thick coupons made of aluminum 2024-T3 were first treated to saturation from both sides with regime #6 and then treated to saturation from one side with the regimes #2-5. The average deflection of the four coupons treated with each regime is presented in Table 2. Table 2 also shows the eigenstrain ε^t_* induced by each regime. It was computed as a function of deflection u_{avg} using the Eqn. (17). We observed a slight difference in deflection of less than 1 % of average in each bunch of the four coupons. It is explained by the presence of initial stresses coming from the manufacturing process.

To characterize the eigenstrain anisotropy (see Section 2.5.3), we treated the 6061-T6 plates following the "wave" pattern with regime #1. The 2024-T3 plates were first treated uniformly with regime #6 and then underwent the "wave" treatment with regime #2. The anisotropy coefficients revealed by the "wave" experiment for the two materials are presented in Table 3. The 6061-T6 plates demonstrated a 4.6 times stronger eigenstrain anisotropy than the 2024-T3 plates.

3.2. The forward problem solver validation

The nine random peening patterns used for validation of the forward problem solver are presented in Figure 11. The patterns and the corresponding

Figure 10: The two target shapes for the 320×320 mm sized panels made of aluminum 2024-T3. The target shapes constituted parts of the upper (blue) and lower (orange) airplane wing skins. The wing was shaped as the NACA 5430 airfoil with the chord length of 500 mm.

simulated shapes were numbered from #1 to #9. Figure 12 (a-f) shows three representative cases demonstrating the smallest, the biggest and an average dimensionless error Ω_z. This figure also traces the local dimensionless mean curvature Hh of each shape, showing that the curvature was qualitatively well simulated. The simulations were performed on the same irregular mesh as that generated by the 3D scanner to allow element-wise curvature comparison. Thus, the irregular mesh was projected onto the initial geometry using the LSCM algorithm and optimized using the L-BFGS algorithm in the same way as during the inverse problem resolution (Figure 3).

The dimensionless error lied in a compact range between 20.5% and 28.5% for seven shapes out of nine. This means that the Hausdorff distance d_H generally increases with Δz, which is illustrated in Figure 12 (g). The shapes #4 and #7 demonstrated significantly smaller Ω_z than the others (8% and 12% respectively), which is explained by the following reason.

The developed jig did not completely prevent deformation of plates during treatment. It clamped the perimeter but let the interior part deform. At the same time, the peening pattern was first fully reproduced from the top side and then from the bottom side. Consequently, when the treatment was applied from the bottom side, the plates were already bent towards the top side. This created an effect of prestress that decreased the eigenstrain in the segments treated from the bottom side [4]. Accordingly, the curvature in

Regime	Pre-treatment (regime)	Material	h (mm)	u_{avg} (mm)	σ_u (mm)	$\varepsilon_*^t \times 10^3$
#1	-	6061-T6	2.05	0.341	0.003	1.19
#2	#6	2024-T3	1.6	0.543	0.005	1.47
#3				0.302	0.015	1.2
#4				0.443	0.004	0.82
#5				0.174	0.007	0.47

Table 2: Results of the eigenstrain measurements performed using the bunches of four 76×19 mm sized aluminum coupons (see Section 2.5.2). The coupons were fixed during peening with an Almen holder, and their deflection was measured with an Almen gage. The thickness of the coupons is denoted by h. The average deflection in each bunch of four coupons is denoted by u_{avg}, and the parameter σ_u describes the standard deviation in deflection. The eigenstrain induced in the top layer is denoted by ε_*^t. In this study we suppose that the eigenstrain ε_*^t equals $-\varepsilon_*^b$, which stands for the eigenstrain induced in the bottom layer.

Material	χ_L	χ_T	χ_*
6061-T6	-0.143	0.193	0.168
2024-T3	0.013	-0.06	0.0365

Table 3: The anisotropy coefficients determined using the "wave" experiment for the two materials. The coefficient χ_* is the average of the absolute values of χ_L and χ_T. The coefficient χ_* was used as the eigenstrain anisotropy coefficient during the simulations.

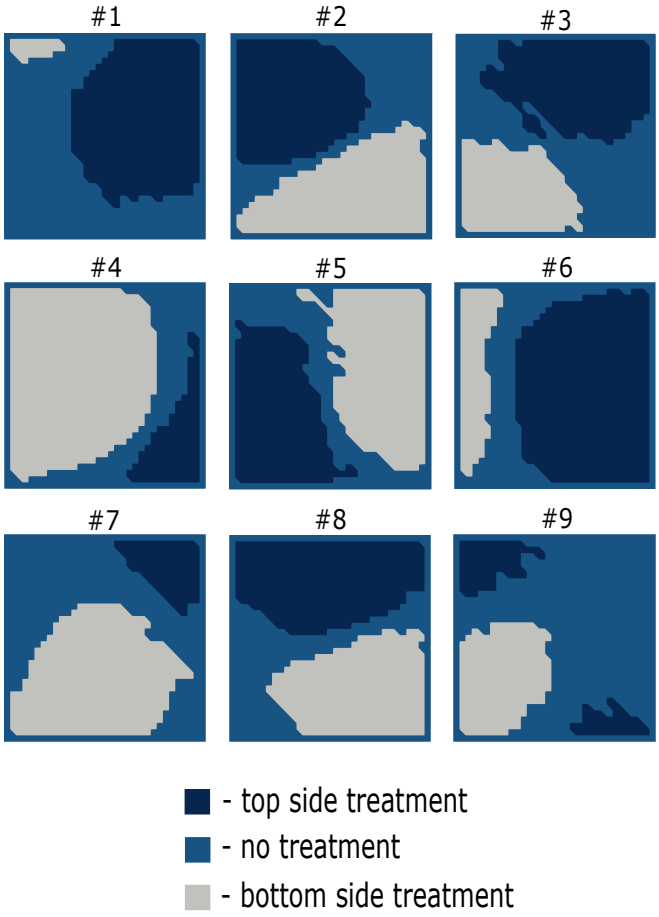

Figure 11: The nine peening patterns that were applied during the experimental forward problem validation. Each pattern implied treatment from both sides. The plates were clamped along their perimeter, so the clamped part did not undergo any treatment. For this reason, each pattern has margins along the plate edges. The patterns were applied using regime #1 without any pretreatment.

these segments was smaller than the simulated one.

The induced prestress varies locally along the plate and is also dependent on the peening pattern. We quantified this effect with the parameter ψ that indicated the ratio of areas treated on the top and bottom sides:

$$\psi = \frac{A_{top} - A_{bot}}{A_{total}}, \tag{18}$$

where A_{top} and A_{bot} are the areas of the segments treated on the top and bottom sides respectively, and A_{total} is the total plate area. Figure 12 (h) plots Ω_z as a function of ψ. This graph shows that the plates #4 and #7 had the smallest ψ among the others, which means that these plates were prestressed less than the others when peened from the bottom side. Accordingly, these shapes showed the smallest Ω_z. Essentially, the problem of an undesirable prestress may be mitigated in practice by constant alternation of the peened sides during treatment. Moreover, this problem becomes less important for stiffened industrial parts, because the stiffeners block bending of the component in the longitudinal direction unless they are not treated themselves [41].

Another issue that increased Ω_z in all the cases consisted in the shot stream width. Thus, the shot stream was not sufficiently narrow to precisely reproduce the borders of the treated segments, which is illustrated in Figure 13. This effect had stronger negative influence on patterns prescribing highly irregular borders to the peened segments. Hence, the plates #5 and #9 demonstrated a high Ω_z while having a relatively small ψ (see Figure 12 h), because the borders of the corresponding peened segments were strongly curved (see Figure 11). On the contrary, the plates #1 and #6 demonstrated a moderate Ω_z while having a large ψ, because the corresponding patterns prescribed smoothly shaped peening segments. The described effect may be mitigated technically with a nozzle that provides a narrower shot stream.

The third source of error consisted in the forces and the moments induced by clamping, which influenced local curvatures inside the treated areas. Thus, the simulations prescribed uniform curvature inside each treated segment, but the experiments revealed that the curvature along the perimeter of the treated segment was higher than in the middle of the segment. This effect was observed on all plates and is visible in Figure 12 (a-f). The influence of this effect depends on the shape of the peening pattern, and its quantification is left for further studies. Nevertheless, we expect the influence of clamping

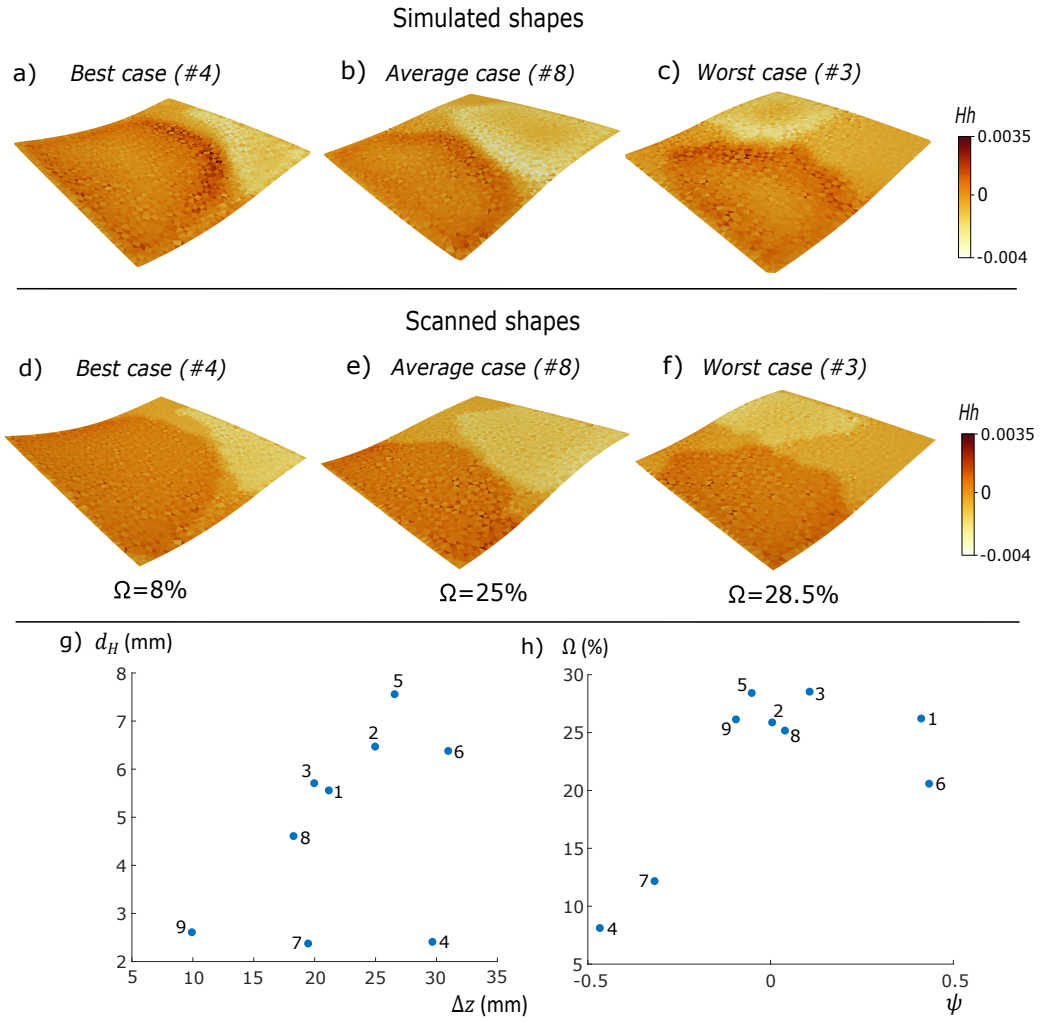

Figure 12: Results of the forward problem validation. We present three representative simulated shapes, which showed the smallest (a), an average (b) and the biggest (c) discrepancy with the experimentally developed shapes. The 3D scanned shapes developed in practice are marked as d), e) and f) respectively. The colormap indicates the local dimensionless mean curvature Hh. The discrepancy was quantified in terms of the dimensionless error Ω_z (Eqn. 13). The graph g) traces the Hausdorff distance d_H for all nine cases depending on the plate deflection. The graph h) traces Ω_z as a function of the parameter ψ, that indicates the difference between the treated areas on the top and bottom sides (Eqn. 18). Each point on the graphs is marked with the number of plate that it corresponds to.

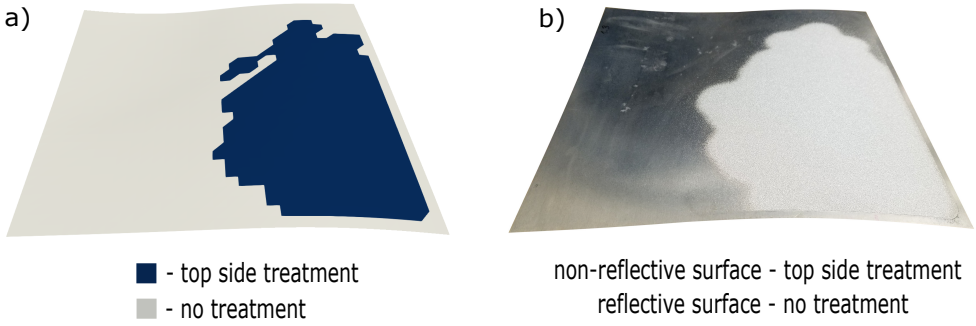

Figure 13: Difference between the prescribed peening pattern and the pattern that was actually applied during treatment. a) The treated area prescribed by the pattern #3 on the top side. b) A photo of the top side of the plate that was treated following pattern #3. The contour of the treated segment is smoother than the one prescribed by the pattern, because the shot stream was too wide to reproduce the contour precisely.

to be weaker for real size industrial panels that have much bigger radii of curvature.

3.3. The inverse problem solver validation

The results of the inverse problem solver validation using the 2024-T3 plates are presented in Figure 14. The fact that these plates were peened from only one side reduced the effect of the undesired prestress. Nevertheless, the outlines of the treated segments were blurred by the wide shot stream, and clamping of the plates altered their curvature, which caused discrepancy between the simulations and the scanned shapes.

The discrepancy between the simulated shapes and the target shapes showed that the fixed peening regimes did not suit perfectly for the chosen target shapes. Thus, the simulated Ω_z equaled 1.2 % for the upper part and 1.4 % for the lower part with the free pattern, that was adjusted iteratively and was free of constraints, and grew up to 5.5 % and 12.9 % respectively with the grouped pattern, that implied only the fixed peening regimes. The main reason for this is that the precise reproduction of the target curvature required gradual transition of intensities from the front line of the wing towards the back line. However, having four predefined peening regimes was not sufficient to ensure smoothness of this transition. Moreover, the highest required eigenstrain for the upper (0.0023) and for the lower (0.0016) parts was higher than that provided by the most intense regime #2 (0.0015). Consequently, the curvature induced by the grouped pattern along the front line

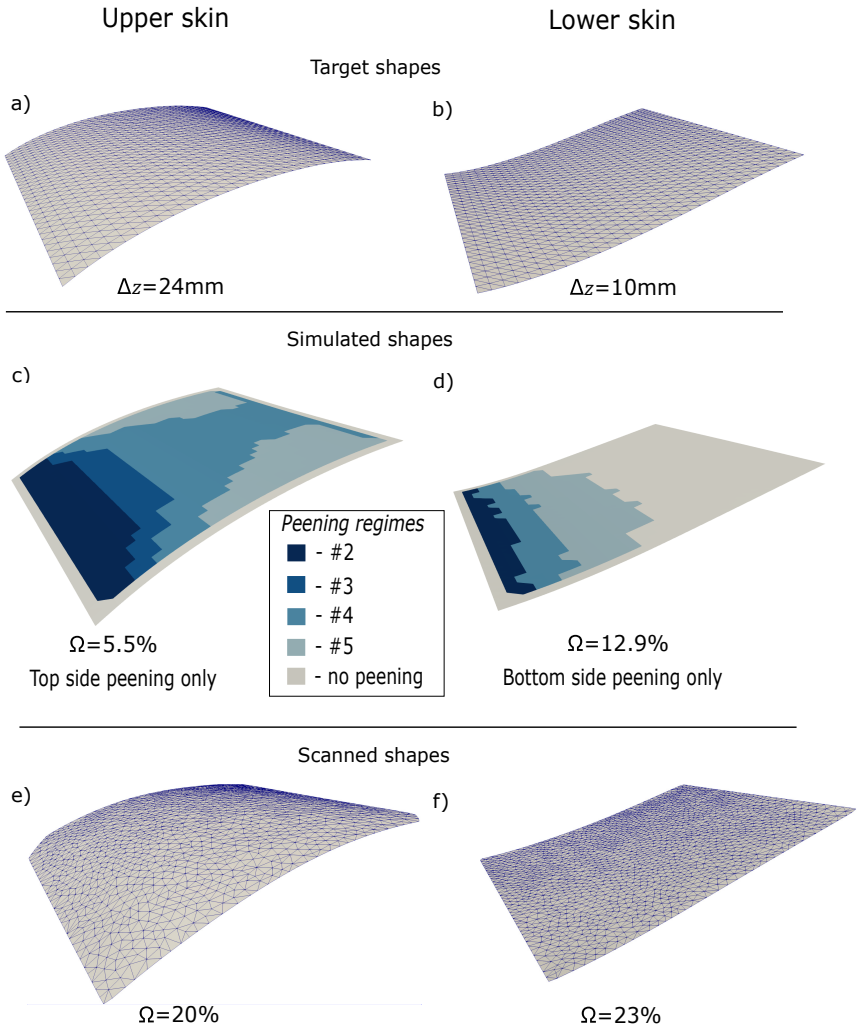

Figure 14: Results of the inverse problem solver validation. The target shapes constitute upper (a) and lower (b) parts of the airplane wing skin reproducing the NACA 5430 airfoil. The inverse problem was solved for both shapes. We simulated deformation induced by the prescribed patterns for the upper (c) and lower (d) skins and compared the simulated shapes with the target shapes. The aluminum plates were treated according to the patterns, and the 3D scans of the upper (e) and lower (f) skins were compared to the target shapes. The deflection Δz is computed as a function of the target shape. The parameter Ω_z describes the dimensionless error with respect to the target shape (Eqn. 13). The plates were made of aluminum 2024-T3 and had the size of $320 \times 320 \times 1.6$ mm. They underwent uniform treatment from both sides with regime #6 before application of the peening patterns.

was inferior to the target one. Figure 15 provides details on the free and the grouped patterns for both target shapes.

The upper plate showed a bistable behaviour after treatment. Thus, the computed final shape appeared to be an unstable state of equilibrium, and the plate tended to curve along the diagonal axis in an unconstrained state. For this reason, we applied a weight on two corners of this plate during scanning, which is a common practice during the accuracy measurements in the peen forming industry. The weight the plate to keep the prescribed longitudinal symmetry, but the two corners had to be discarded from the numerical model provided by the 3D scanner (see Figure 14).

We used the two plates to assemble a physical model of the NACA 5430 airfoil, which is presented in Figure 16. The forward and the back parts of the model wing, which are colored in black in Figure 10, were printed

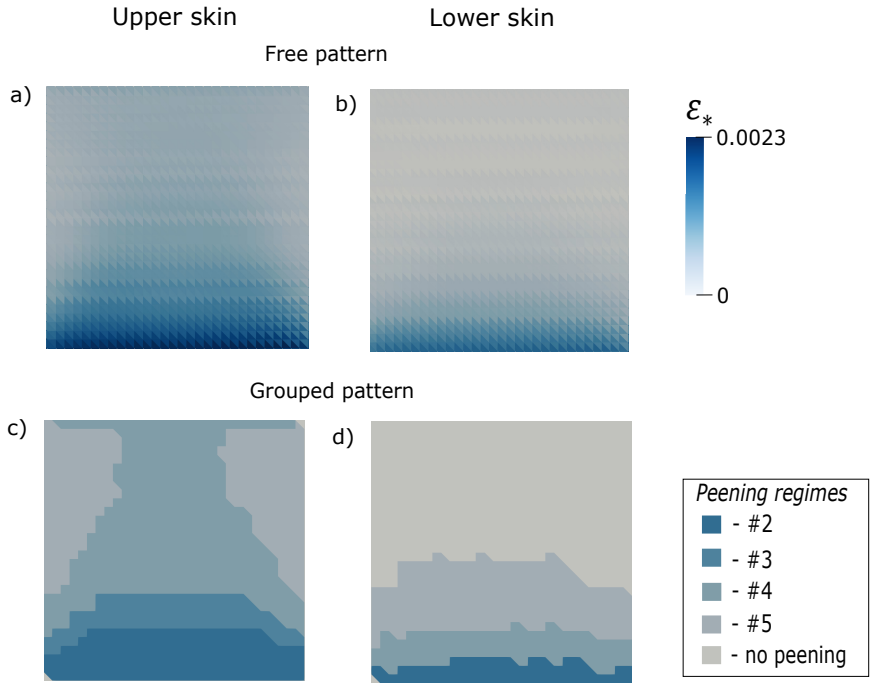

Figure 15: The eigenstrain patterns prescribed by the inverse problem to shape the airplane wing skin parts. Before grouping, the patterns assign gradual transition of the eigenstrain along the plate surface to shape the upper (a) and the lower (b) skins. The grouping process divides the patterns for the upper (c) and lower (d) parts into segments with constant eigenstrain. The eigenstrain in the grouped segments corresponds to the one induced by the fixed peening regimes.

Figure 16: The model of an airplane wing skin shaped as the NACA 5430 airfoil with a chord length of 500mm. The upper and lower skins were shaped using the shot peen forming, and the forward and the back parts (black) were printed in 3D. The structure is assembled using binding barrels and screws.

in 3D using an FDM printer charged with the PLA plastic. These parts also served as supports for the aluminum plates. The plates were drilled and assembled with the printed parts using binding barrels and screws. The constraints induced by the binding have eliminated the shaping error, so the plates perfectly fit the NACA profile. This situation is often the case in industry, where the parts are shaped up to a pre-defined tolerance, and the error is entirely eliminated only when the part is installed.

4. Conclusion

We developed a complete workflow for the shot peen forming automation. We generate the numerical peening pattern and we automatically translate it into a program for the shot peening robot. The program admits application of multiple peening regimes following complex patterns and thus allows to shape complex doubly-curved shapes. The workflow implies preliminary characterization of the shot stream effect in terms of eigenstrain and characterization of the eigenstrain anisotropy. These preliminary stages are necessary to generate the peening pattern and the nozzle paths. Simple yet efficient procedures were designed for this purpose.

The workflow was validated experimentally. The validation implied treatment following randomly generated patterns and shaping skins of a model airplane wing. The treatment was performed at high Almen intensities of 10.9-23.5A to reveal all possible errors appearing with large deformations. The validation showed promising results but revealed an error between the simulated shapes and the practically developed shapes from 8% to 28.5% of

the total deflection. We expect this error to be smaller for industrial parts that have bigger radii of curvature and include stiffeners, because these components are less subjected to the undesirable prestress and to the influence of clamping supports. The inverse problem solver validation also emphasized the importance of an optimal choice of the peening regimes for each target shape.

The vast experimental campaign indicated directions for the workflow improvement. The simulation error was provoked by an incomplete consistency between the simulated and the real peening conditions. The major difference lies in the fact that the software simulates immediate application of the peening treatment from both sides, while in practice it was first fully applied from one side and then from the other. The future experiments will imply uniform application of the pattern from both sides, i.e., alternation of the peened sides after each pass of the peening nozzle. In addition, the peening nozzle will be modified in order to provide a narrower shot stream and thus to reproduce the pattern more accurately. The effect of clamping on the eigenstrain distribution will also be quantified.

5. Acknowledgements

The authors gratefully acknowledge financial support from The Fonds de Recherche du Québec – Nature et Technologies (FRQNT), from The Aluminium Research Centre – REGAL, and from the industrial partner of this project – Aerosphere Inc. The authors also acknowledge the consulting support provided by Aerosphere Inc. An important contribution to this project was made by Raphaël Paradis, who fabricated the peen forming fixture during his internship at the Aerospace Technology Center (CTA), and by Nada Abbassi, who performed the experimental manipulations for validation of the inverse problem solver during her internship at Polytechnique Montreal.

Appendix A. Proportionality between the dimensionless load and curvature

We performed a specific series of simulations in order to find the proportionality constant μ relating κh and Γ_B (Eqn. 15). Namely, we took a range of the dimensionless loads Γ_B and simulated its application on aluminum coupons of size 76×19 mm and various thickness h. All in all, 100 testcases for Γ_B ranging between 0 and 0.008 were simulated. For each testcase, ε^t_*

was positive and ε_*^b was negative, but the ratio $\varepsilon_*^t/\varepsilon_*^b$ was chosen randomly between -1 and 0. The material was considered plastically isotropic. Additionally, the thickness h ranged randomly from 2 to 4 mm for each testcase. The Poisson's ratio ν was fixed equal to 0.33, that is a typical value for aluminum. We meshed the coupons with 760 triangular elements and solved the forward problem as described in Section 2.1.3. For all the testcases, the curvature κ measured at the center of the coupon varied by less than 0.015% in different directions, that proves the results presented in Ref. [22].

Appendix B. Influence of the eigenstrain anisotropy

The eigenstrain anisotropy is majorly caused by the material properties, but its influence is not always perceptible during uniform treatment of the 76×19 mm coupons. Thus, the 1.6 mm and 2.06 mm thick coupons develop the same local curvature in both directions when treated with the regimes described in Table 1. This is explained by the fact that the curvature of uniformly peened rectangular specimens depends on [21] [22]:

$$\overline{\Gamma}_B = \Gamma_B \frac{D^2}{h^2}, \tag{B.1}$$

where D is the characteristic length of the specimen. Namely, rectangular specimens adopt spherical shape for low values of $\overline{\Gamma}_B$ independently of the eigenstrain anisotropy. Thus, the applied treatment was not intense enough to make the 76×19 mm sized coupons develop different curvatures in the L- and T-directions. The 320×320mm sized plates have 17.7 times bigger $\overline{\Gamma}_B$ than the coupons of the same thickness treated with the same regime. Consequently, this type of plates was used for determination of the eigenstrain anisotropy.

Appendix C. Influence of pre-treatment on the induced eigenstrain

We performed additional measurements to characterize the eigenstrains induced in the 2024-T3 panels that did not undergo the preliminary double-side treatment with regime #6. First, we measured the eigenstrains induced in the 76×19 mm coupons cut of the same plates (see Section 2.5.2). The results of this measurement are summarized in Table C.4. The induced deflection of the coupons was bigger than in the case with pre-treatment, so the

Regime	u_{avg} (mm)	σ_u (mm)	$\varepsilon^t_* \times 10^3$	Increase in ε^t_*
#2	0.706	0.008	1.91	169%
#3	0.629	0.015	1.7	92%
#4	0.582	0.012	1.58	42%
#5	0.467	0.001	1.26	30%

Table C.4: Results of the additional eigenstrain measurements performed using the bunches of four $76 \times 19 \times 1.6$ mm sized aluminum coupons (see Section 2.5.2). The coupons were made of aluminum 2024-T3 and did not undergo any pre-treatment. They were fixed during peening with an Almen holder, and the deflection was measured with an Almen gage. The average deflection in each bunch of four coupons is denoted by u_{avg}, and the parameter σ_u describes the standard deviation in deflection. The eigenstrain induced in the top layer is denoted by ε^t_*. The right column shows the increase in ε^t_* with respect to the pre-treated coupons peened with the same regimes (Table 2).

induced eigenstrains were bigger as well. This phenomenon is explained by hardening of the surface generated by the pre-treatment, which is discussed for example in Ref. [42]. The influence of hardening was more significant for less intense peening regimes (Table 1). Thus, the absence of pre-treatment increased the eigenstrain induced by the regime #5 by 169%, while the eigenstrain induced by the regime #2 was only increased by 30%. The graphical comparison of the eigenstrain induced in both cases is presented in figure C.17.

Next, we characterized the eigenstrain anisotropy using the "wave" experiment (see Section 2.5.3). Thus, we treated two 2024-T3 panels following the "wave" pattern with regime #2 without pre-treatment. The experiment revealed a mild eigenstrain anisotropy, which is characterized in terms of the coefficient χ_* in Table C.5. The principal eigenstrain direction has changed with respect to the case with pre-treatment, but the value of χ_* is of the order of 10^{-3}, which means that the eigenstrain is almost isotropic. Given that the eigenstrain anisotropy demonstrated by the pre-treated plates was mild as well (Table 3), we conclude that the pre-treatment did not have a tangible influence on this parameter.

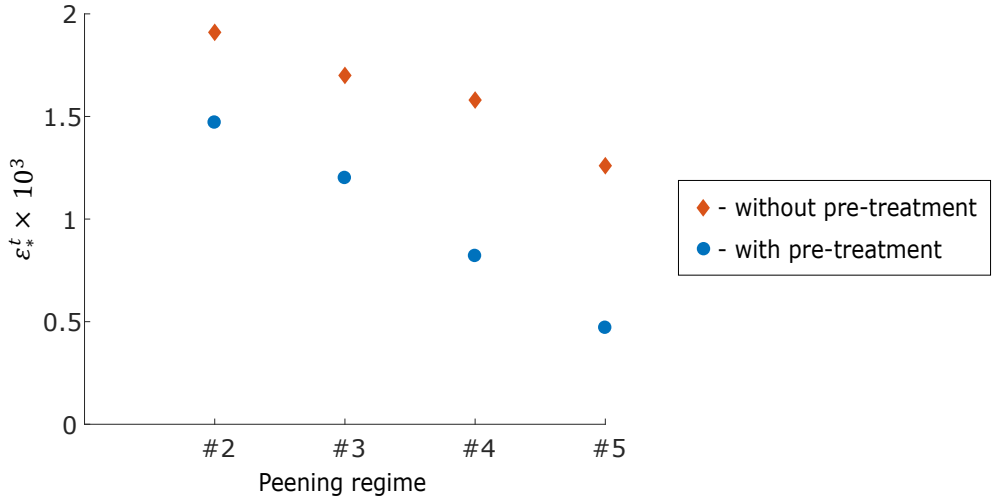

Figure C.17: Graphical comparison of the eigenstrain ε_*^t induced by the same peening regimes on pre-treated and not pre-treated coupons. The coupons had the size of 76 $\times$ 19 $\times$ 1.6 mm and were made of aluminum 2024-T3. The pre-treatment was done using the regime #6. The parameters describing each peening regime are presented in Table 1. The exact values of ε_*^t for each case are presented in Tables 2 and C.4.

χ_L	χ_T	χ_*
-0.013	0.003	0.008

Table C.5: The anisotropy coefficients determined using the "wave" experiment for the 2024-T3 plates that were not pre-treated. The "wave" pattern was applied using the regime #2. The eigenstrain anisotropy coefficient χ_* is the average of the absolute values of χ_L and χ_T.

References

[1] S. Ramati, S. Kennerknecht, G. Levasseur, Single piece wing skin utilization via advanced peen forming technologies, Proceedings of the ICSP7, Warsaw (1999).
URL http://www.aerosphere.ca/docs/ICSP-7.pdf

[2] J. Merino, A. Patzelt, A. Steinacher, M. Windisch, G. Heinrich, R. Forster, C. Bauer, Ariane 6-Tanks and structures for the new european launcher, Deutsche Gesellschaft für Luft-und Raumfahrt-Lilienthal-Oberth eV, 2017.
URL https://www.dglr.de/publikationen/2017/450255.pdf

[3] F. Wüstefeld, W. Linnemann, S. Kittel, Towards peen forming process automation, Shot Peening (2006) 44.
URL https://www.shotpeener.com/library/detail.php?anc=2002007

[4] H. Y. Miao, P. A. Faucheux, M. levesque, F. Gosselin, Residual stress measurements of conventional and stress peen formed 2024-t3 aluminum sheets (Apr 2021). doi:10.31224/osf.io/c5t9r.
URL engrxiv.org/c5t9r

[5] A. Friese, Ksa develops new automated peen forming for wing skins, The Shot Peener magazine 16 (2006).
URL https://www.shotpeener.com/library/pdf/2006031.pdf

[6] Z. Chen, F. Yang, S. Meguid, Realistic finite element simulations of arc-height development in shot-peened almen strips, Journal of Engineering Materials and Technology 136 (2014) 041002. doi:10.1115/1.4028006.

[7] T. Mura, Micromechanics of defects in solids. vol. 3, Springer Science & Business Media 580 (1987) 21.

[8] A. Korsunsky, The modelling of residual stresses due to surface peening using eigenstrain distributions, The Journal of Strain Analysis for Engineering Design 40 (2005) 817–824. doi:10.1243/030932405X30984.

[9] P. A. Faucheux, F. P. Gosselin, M. Lévesque, Simulating shot peen forming with eigenstrains, Journal of Materials Processing Technology 254 (2018) 135–144. doi:https://doi.org/10.1016/j.jmatprotec.

2017.11.036.
URL https://www.sciencedirect.com/science/article/pii/S0924013617305563

[10] A. Korsunsky, Residual elastic strain due to laser shock peening: Modelling by eigenstrain distribution, Journal of Strain Analysis for Engineering Design 41 (2006) 195–204. doi:10.1243/03093247JSA141.

[11] W. Siguerdidjane, F. Khameneifar, F. P. Gosselin, Efficient planning of peen-forming patterns via artificial neural networks, Manufacturing Letters 25 (2020) 70–74. doi:https://doi.org/10.1016/j.mfglet.2020.08.001.
URL https://www.sciencedirect.com/science/article/pii/S2213846320301395

[12] W. M. van Rees, E. A. Matsumoto, A. S. Gladman, J. A. Lewis, L. Mahadevan, Mechanics of biomimetic 4d printed structures, Soft matter 14 (43) (2018) 8771–8779. doi:10.1039/C8SM00990B.

[13] V. Sushitskii, W. M. van Rees, M. levesque, F. Gosselin, Determination of optimal shot peen forming patterns using the theory of non-euclidean plates (Dec 2021). doi:10.31224/osf.io/j36ku.
URL engrxiv.org/j36ku

[14] X. Kang, T. Wang, J. Platts, Multiple impact modelling for shot peening and peen forming, Proceedings of the Institution of Mechanical Engineers, Part B: Journal of engineering manufacture 224 (2010) 689–697. doi:10.1243/09544054JEM1672.

[15] S. Zhang, A. Venter, W. Vorster, A. Korsunsky, High-energy synchrotron x-ray analysis of residual plastic strains induced in shot-peened steel plates, The Journal of Strain Analysis for Engineering Design 43 (4) (2008) 229–241. doi:https://doi.org/10.1243/03093247JSA341.

[16] A. Levers, A. Prior, Finite element analysis of shot peening, Journal of Materials Processing Technology 80-1 (1998) 304–308. doi:10.1016/S0924-0136(98)00188-5.

[17] T. Wang, M. Platts, A. Levers, A process model for shot peen forming, Journal of Materials Processing Technology 172 (2006) 159–162. doi:10.1016/j.jmatprotec.2005.09.006.

[18] M. B. Prime, Amplified effect of mild plastic anisotropy on residual stress and strain anisotropy, International Journal of Solids and Structures 118-119 (2017) 70–77. doi:https://doi.org/10.1016/j.ijsolstr.2017.04.022.
URL https://www.sciencedirect.com/science/article/pii/S0020768317301725

[19] V. K. Barnwal, A. Tewari, K. Narasimhan, S. K. Mishra, Effect of plastic anisotropy on forming behavior of aa-6061 aluminum alloy sheet, The Journal of Strain Analysis for Engineering Design 51 (7) (2016) 507–517. doi:10.1177/0309324716655727.

[20] F. Bron, J. Besson, A yield function for anisotropic materials application to aluminum alloys, International Journal of Plasticity 20 (2004) 937–963. doi:10.1016/j.ijplas.2003.06.001.

[21] P. A. Faucheux, Simulating shot peen forming with eigenstrains, Ph.D. thesis, Polytechnique Montreal (December 2019).
URL https://publications.polymtl.ca/4189/

[22] H. Y. Miao, M. levesque, F. Gosselin, Peen forming and stress peen forming of 2024-t3 aluminum sheets. part 2: eigenstrain analysis (Apr 2021). doi:10.31224/osf.io/kwbj6.
URL engrxiv.org/kwbj6

[23] H. Y. Miao, M. Lévesque, F. P. Gosselin, Shot peen forming pattern optimization to achieve cylindrical and saddle target shapes: The inverse problem, CIRP Journal of Manufacturing Science and Technology 36 (2022) 67–77. doi:https://doi.org/10.1016/j.cirpj.2021.11.003.

[24] K. Han, D. Owen, D. Peric, Combined finite/discrete element and explicit/implicit simulations of peen forming process, engineering computations (2002). doi:https://doi.org/10.1108/02644400210413667.

[25] R. VanLuchene, E. Cramer, Numerical modeling of a wing skin peen forming process, Journal of materials engineering and performance 5 (6) (1996) 753–760. doi:https://doi.org/10.1007/BF02646910.

[26] W. M. van Rees, E. Vouga, L. Mahadevan, Growth patterns for shape-shifting elastic bilayers, Proceedings of the National Academy of Sci-

ences 114 (44) (2017) 11597–11602. doi:https://doi.org/10.1073/pnas.1709025114.

[27] P. G. Ciarlet, An introduction to differential geometry with applications to elasticity, Journal of Elasticity 78 (1) (2005) 1–215. doi:https://doi.org/10.1007/s10659-005-4738-8.

[28] B. O'neill, Elementary differential geometry, Elsevier, 2006.

[29] M. P. Do Carmo, Differential geometry of curves and surfaces: revised and updated second edition, Courier Dover Publications, 2016.

[30] D. C. Liu, J. Nocedal, On the limited memory bfgs method for large scale optimization, Mathematical programming 45 (1) (1989) 503–528. doi:https://doi.org/10.1007/BF01589116.

[31] R. Tamstorf, E. Grinspun, Discrete bending forces and their jacobians, Graphical Models 75 (2013) 362–370. doi:10.1016/j.gmod.2013.07.001.

[32] B. Lévy, S. Petitjean, N. Ray, J. Maillot, Least squares conformal maps for automatic texture atlas generation, ACM transactions on graphics (TOG) 21 (3) (2002) 362–371.
URL https://www.cs.jhu.edu/~misha/Fall09/Levy02.pdf

[33] G. Garg, V. Kuts, G. Anbarjafari, Digital twin for fanuc robots: Industrial robot programming and simulation using virtual reality, Sustainability 13 (2021) 10336. doi:10.3390/su131810336.

[34] R. T. Rockafellar, R. J.-B. Wets, Variational analysis, Vol. 317, Springer Science & Business Media, 2009.
URL https://sites.math.washington.edu/~rtr/papers/rtr169-VarAnalysis-RockWets.pdf

[35] S. Umeyama, Least-squares estimation of transformation parameters between two point patterns, IEEE Transactions on Pattern Analysis and Machine Intelligence 13 (4) (1991) 376–380. doi:10.1109/34.88573.

[36] D. Kirk, Shot peening, Aircraft engineering and aerospace technology (1999).
URL https://www.shotpeener.com/library/pdf/1999003.pdf

[37] Test strip, holder, and gage for shot peening, Standard SAE J442, SAE International (2009).
URL https://www.sae.org/standards/content/j442_201302/

[38] D. Kirk, The curvature of peened almen strips and its applications, The Shot Peener magazine 32 (4) (2018).
URL https://www.shotpeener.com/library/pdf/2018043.pdf

[39] H. Li, Y. Lu, Z. Han, X. Guo, Y. Xu, X. Xu, J. Tao, The shot peen forming of fiber metal laminates based on the aluminum-lithium alloy: Deformation characteristics, Composites Part B: Engineering 158 (2019) 279–285. doi:https://doi.org/10.1016/j.compositesb.2018.09.085.
URL https://www.sciencedirect.com/science/article/pii/S1359836818323370

[40] J. Moran, An introduction to theoretical and computational aerodynamics, Courier Corporation, 2003.

[41] M. Wang, Y. Zeng, X. Bai, X. Huang, Shot peen forming on aluminum alloy saddle shape integral panels with stiffeners, Proceedings of the ICSP-13, Montreal (2017).
URL https://www.shotpeener.com/library/detail.php?anc=2017138

[42] T. Chaise, J. Li, D. Nélias, R. Kubler, S. Taheri, G. Douchet, V. Robin, P. Gilles, Modelling of multiple impacts for the prediction of distortions and residual stresses induced by ultrasonic shot peening (usp), Journal of Materials Processing Technology 212 (10) (2012) 2080–2090. doi:https://doi.org/10.1016/j.jmatprotec.2012.05.005.
URL https://www.sciencedirect.com/science/article/pii/S0924013612001513